

Simulations for Mid-IR Photon Generation in Gas-filled Hollow-core Fibre by Four-wave Mixing

Author:

Jack Morse

Assessor:

Prof Jonathan Knight

Supervisor:

Dr Peter Mosley

Abstract

Four-wave mixing (FWM) is a pertinent tool for photon-generation in the mid-IR, subject to the appropriate energy conservation and phase-matching conditions. Using anti-resonant hollow-core fibre filled with a noble gas, we theoretically tailor the dispersion to find FWM solutions beyond $3\text{ }\mu\text{m}$, exploiting the $\chi^{(3)}$ nonlinearity of the filling gas. Through simulations, we report a $3.07\text{ }\mu\text{m}$ solution with a $1.55\text{ }\mu\text{m}$ pump, for reasonable fibre parameters. We discuss the possibility of extending these solutions to longer wavelengths by exploiting the nonlinearity-power product in the phase-matching equation. Although the fibre provides a long confinement length for phase-matching to build up in principle, we comment on the overall efficiency for some solutions which exist close to the high-loss resonances of the fibre. We also provide details of two fibre dispersion measurement techniques and present their respective results.



BSc Final Year Project Report
Department of Physics

Tuesday 7th May 2024

Contents

Acknowledgements	ii
Abbreviations	ii
List of Figures	ii
1 Introduction	1
2 Dispersion in Optical Fibres	1
2.1 Formulation of theory	1
2.1.1 Group velocity dispersion	3
3 Hollow-core Fibre	3
3.1 Description of anti-resonant HCF	4
3.2 Modelling dispersion in HCF	5
3.3 Extending the model: Gas-filled HCF	6
4 Methods for Measuring Fibre Dispersion	7
4.1 Theory of spectral interferometry	7
4.1.1 Zero-delay frequency	7
4.2 Manual dispersion measurement	8
4.3 Fourier transform spectral interferometry	10
5 Four-wave Mixing	12
5.1 Introduction to nonlinear optics	12
5.2 Scalar theory of four-wave mixing	13
5.2.1 Phase-matching in hollow-core fibre	13
6 Simulation Results	14
6.1 Dependence on model parameters	15
7 Conclusion and Outlook	16
References	16

Acknowledgements

My sincere thanks go first to Molly, my project partner, for her support, knowledge, commitment, and sense of humour in making this project jointly enjoyable and successful. I am also extremely grateful to Mat Olszewski for his invaluable guidance and support in the lab. A special acknowledgement goes to Prof David Bird for his expertise and discussion in enhancing our modelling to better incorporate the effects of negative curvature. Last but not least, my genuine thanks to Pete, our supervisor, whose passion for the subject and encouragement has pushed us to deliver our best work and learn much along the way.

Abbreviations

FFT	: <i>Fast Fourier transform</i>
FUT	: <i>Fibre under test</i>
FWM	: <i>Four-wave mixing</i>
GD	: <i>Group delay</i>
GDD	: <i>Group delay dispersion</i>
GVD	: <i>Group velocity dispersion</i>
HCF	: <i>Hollow-core fibre</i>
IR	: <i>Infrared</i>
PBG	: <i>Photonic band gap</i>
PCF	: <i>Photonic crystal fibre</i>
SI	: <i>Spectral interferometry / interference</i>
TIR	: <i>Total internal reflection</i>
ZDW	: <i>Zero dispersion wavelength</i>

List of Figures

1	ARROW guidance mechanism & HCF geometry	4
2	Hollow-core dispersion model	6
3	Dispersion measurement setup	8
4	Manual dispersion measurement results	9
5	FTSI dispersion measurement of HCF	11
6	Four-wave mixing illustration	12
7	FWM phase-matching solutions	14
8	Effect of parameter variation on phase-matching	15

1 Introduction

In recent years there has been significant interest in mid-infrared (mid-IR) lasers, which persist in promising exciting applications in medical sensing [1], environmental monitoring [2], laser-wakefield acceleration [3], and quantum sensing. For instance, ground-to-satellite communications could be significantly improved by the distribution of mid-IR signals due to the reduction in atmospheric absorption/scattering [4]. In the past few decades, mid-IR fibre lasers [5], solid-state lasers [6], and nonlinear sources have all been used to produce useful coherent light in the mid-IR.

Four-wave mixing (FWM) in hollow-core fibres (HCF) is a promising approach. In 2013, Azhar *et al.* successfully demonstrated FWM solutions up to 1.5 μm with an 800 nm centered pump in a Kagomé fibre filled with xenon gas up to 150 bar [7]. More recently, Ciriolo *et al.* produced pulses in the visible inside a hollow fibre with low pressure (~ 1 bar) gases (Kr, N₂, CO₂), and also provided numerical evidence for broad-band mid-IR pulses centered on 3.1 μm , seeded with 800 nm and 1.3 μm centered beams [8].

In this work, we investigate theoretically the generation of mid-IR light from a single pump beam in an anti-resonant HCF filled with a noble gas through degenerate FWM. Crucially, noble gases avoid Raman noise, since they possess no roto-vibrational modes for the fields to couple to. The gas provides high $\chi^{(3)}$ nonlinearity which permits the FWM process, and the fibre provides the large confinement distance for efficient phase-matching to accumulate in principle. We can tailor the dispersion of the fibre by varying parameters such as capillary thickness, core radius, and gas pressure, to achieve phase-matching far detuned from the pump. The results we obtained indicate that farther detuning will be hindered by higher loss, as the solutions we identified lie close to the resonances of the fibre. We do however discuss possible ways to overcome this, for instance by exploiting the high optical powers the gas and the hollow-core fibres are capable of sustaining.

The report is structured as follows. In Section 2, we introduce some relevant concepts in dispersion; in Section 3 we describe the anti-resonant HCF guidance mechanism and develop a dispersion model based on the work of Zeisberger *et al.* [9]. We then take a detour and describe two methods for measuring fibre dispersion, applying the second, Fourier transform spectral interferometry, to a hollow-core fibre for which we compare the result to the model. In Section 5 a brief motivation and description of nonlinear optics is provided, with an emphasis on the four-wave mixing process. Finally in Section 6 we present the results of our simulations, providing the phase-matched mid-IR solutions and their dependence on the model parameters.

2 Dispersion in Optical Fibres

In this section, we give a brief treatment of the relevant theory describing dispersion, introducing useful terms such as the accumulated spectral phase and group velocity dispersion, which are referred to throughout.

2.1 Formulation of theory

Chromatic dispersion describes how the refractive index function of a material depends on the frequency of light propagating through it. A first principles approach to explaining dispersion

may be achieved by modelling the bound electrons and ionic dipoles in a solid as connected by springs driven by an incoming radiation field, and solving for the output field due to the effect of the oscillating charges – see for instance Fox (2010) [10]. In practice however, the *effect* of dispersion is readily described by multiplying the initial light field $\hat{E}(\omega)$, defined in frequency, by a phasor $\exp(i\Phi(\omega))$ after propagating a distance L through a medium. Here $\Phi(\omega)$ is the accumulated spectral phase, which is related to the longitudinal component of the wave-vector β through $\beta = \Phi/L$. β is also referred to as the propagation constant, or in this context sometimes the spectral phase per unit length. It is natural to relate Φ to standard quantities by a Taylor expansion centered around angular frequency ω_0 [11]:

$$\Phi(\omega) = \Phi(\omega_0) + \Phi'(\omega_0)(\omega - \omega_0) + \frac{1}{2}\Phi''(\omega_0)(\omega - \omega_0)^2 + \frac{1}{6}\Phi'''(\omega_0)(\omega - \omega_0)^3 + H.O.T, \quad (1)$$

where $\Phi(\omega_0)$ is an absolute phase term, $\Phi'(\omega_0)$ is the group delay (GD), $\Phi''(\omega_0)$ is the group delay dispersion (GDD), $\Phi'''(\omega_0)$ is the third-order dispersion (TOD), and *H.O.T* stands for higher-order terms. The TOD and higher-order derivatives of Φ are generally known as higher-order dispersion (HOD). In some cases, HOD terms are needed, for instance when the spectral range is large, meaning more coefficients in the Taylor expansion are needed to maintain accurate convergence.

The electric field in time is related to the electric field in frequency through the Fourier transform: $E(t) \xleftrightarrow{\mathcal{F}} \hat{E}(\omega)$. Often, dispersion is described by considering how the phase velocity v_p varies as a function of frequency. The phase velocity is related to the group velocity v_g by

$$v_g := \frac{\partial \omega}{\partial \beta} = v_p + \beta \frac{\partial v_p}{\partial \beta} \quad (2)$$

$$= \frac{v_p^2}{v_p - \omega \frac{\partial v_p}{\partial \omega}}. \quad (3)$$

Generally, the group velocity will differ from the phase velocity, i.e. when $\partial v_p / \partial \omega \neq 0$. The group velocity is related to the GD (units seconds) by the simple speed-time relation

$$\Phi' = \frac{L}{v_g}, \quad (4)$$

where Φ' is the GD by its definition and L is the length of the material. Note the primes will be used to represent differentiation with respect to angular frequency. When the GD is constant and there are no higher-order terms, a laser pulse maintains its chirp (which may be zero) with each frequency delayed by the same amount. This can be seen directly through the Fourier transform since the time-shift formula tells us that a linear spectral phase corresponds to a constant delay in time. However, if there are higher order terms, we will see a delay which depends on the frequency. The rate at which this dispersion occurs is described by the GDD which is considered next.

From Eq. (1), the GDD (units seconds squared) is the derivative with respect to angular frequency of the GD. Therefore, from Eq. (4) we find

$$\Phi'' = L\beta_2 = L \left(\frac{1}{v_g} \right)', \quad (5)$$

where $\beta_2 (= \beta'')$ is the group velocity dispersion (GVD).

At this point, we define the dispersion parameter D , which is often used synonymously with the GVD, as

$$D = \frac{1}{L} \frac{\partial}{\partial \lambda} \Phi'. \quad (6)$$

The units for D are conventionally expressed in ps/(nm · km), and can thus be interpreted as the delay in picoseconds accumulated per nanometer wavelength change after a kilometer of propagation.

In the case of optical fibres which we discuss in later sections, we highlight that there is in reality wave-guide dispersion and material dispersion, but that these are all contained in the effective dispersion which is usually measured in any experiment.

2.1.1 Group velocity dispersion

An important distinction is made about the sign of the second-order dispersion: We denote $\beta_2 > 0$ (equivalently $D < 0$) as the *normal* dispersion regime and $\beta_2 < 0$ (equivalently $D > 0$) as the *anomalous* dispersion regime. When an initially unchirped pulse propagates through a material's normally dispersive region it will obtain a positive linear chirp, whereby higher frequencies travel slower through the material than lower ones. The opposite is true in the case of anomalous dispersion.

Many materials, including silica glass (SiO_2) are normally dispersive in the visible region. The point at which the dispersion changes sign (i.e. equals zero) has a special name; it is known as the zero dispersion wavelength (ZDW).

Precise tailoring of dispersion profiles is sometimes fundamentally important, and dispersion control has impacted many areas from high-power lasers to minimising data loss over long-range communication. It is also essential to facilitating many nonlinear interactions, particularly in optical fibre, as we will see in later sections.

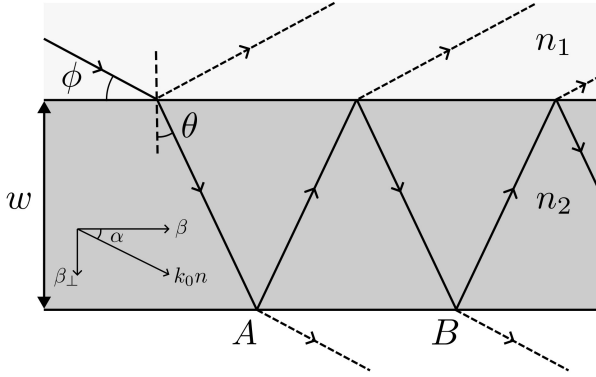
3 Hollow-core Fibre

Optical wave-guides were first developed in the late 1960s in the form of step-index optical fibres, which confine light to the core by total internal reflection (TIR). Since then, these fibres have become the industry standard and form the basis of our global telecommunications network, enabling everything from the trading of stocks to the transmission of data through the Internet. They have facilitated the rapid global development that has occurred since, with their main benefit being their low signal loss over long-range transmission.

Hollow-core optical fibres (HCF) work on entirely different guidance principles to step-index fibres. There are broadly two guidance mechanisms for HCFs: Photonic band gap (PBG) and anti-resonance. The former guides through a periodic microstructure that sets up 'allowed' transmission bands that are generally narrow and highly sensitive to manufacturing tolerances [12, 13].

On the other hand, anti-resonant HCFs (AR-HCF) guide through an interference effect in thin capillary walls. Since the first reported fabrication of these fibres in 2011 [14], AR-HCF designs have improved to the extent that they now rival conventional single-mode fibres in terms of propagation loss at telecommunication wavelengths [15]. This is largely due to the

(a)



(b)

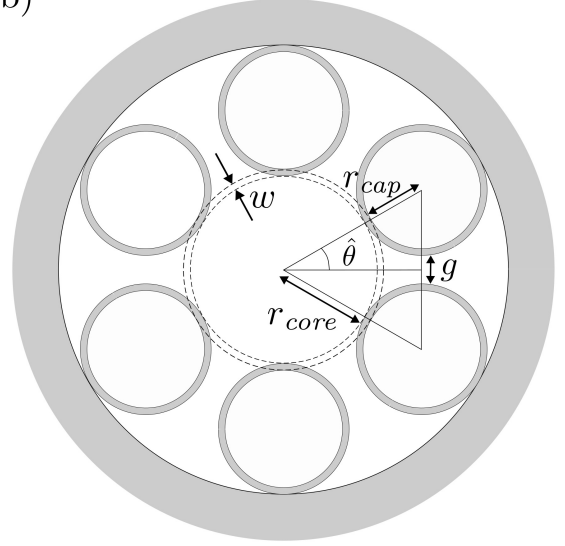


Figure 1: (a) Geometry of anti-resonant reflecting optical wave-guide (ARROW) with incident ray at grazing angle ϕ . The resonance condition is that the transverse phase difference accumulated for rays leaving the core (index n_1) through the capillary (index n_2 , thickness w) at points A and B is an integer multiple of 2π . Here, the components of the wave-vector are shown with β being the longitudinal component and β_\perp the transverse component. (b) Anti-resonant HCF with $M = 6$ rings. The angle $\hat{\theta}$ in the figure is π/M and the closest gap between capillaries g is deduced through the construction lines shown.

use of negative curvature whereby the guiding walls are negatively curved relative to the core [16]. The dispersion profile of AR-HCFs is readily explained by approximate models as will be shown in Section 3.2, and away from the resonances the GVD of these fibres is generally flat.

A key advantage of HCFs over conventional fibres is their high-power operation, since the majority (over 99.99%) of the guided light is confined to the core region [17]. Furthermore, the anti-resonance condition combined with the fact that most of the light is not propagating in the glass layer means that these fibres can guide well into the mid-IR, where traditional solid-core silica-based fibres lose their transparency due to multi-phonon absorption.

In this work, we consider a revolver-type AR-HCF (which we will refer to as HCF). We let M be the number of capillaries arranged in a circular array around a gas-filled (or otherwise empty) core, for which we consider $M = 6$, as depicted in Fig. 1 (b).

3.1 Description of anti-resonant HCF

The anti-resonant reflecting guidance mechanism for optical wave-guides, abbreviated to ARROW [18], explains geometrically how guidance inside the hollow-core is achieved by considering a phase-matching condition for light leaving the fibre perpendicular to the core.

The idea is to consider a ray of grazing angle ϕ inside the core, as can be assumed for the fundamental mode, incident on the thin-wall capillary where the index profile between the core n_1 and capillary n_2 satisfies $n_2 > n_1$ (see Fig. 1 (a)). If this condition is not satisfied the interaction can simply be considered by TIR, as is the case in conventional fibres. Once the light enters the capillary, it behaves like a thin film Fabry-Perot cavity. Such a cavity is

characterised by its narrow transmission bands and wide anti-resonant bands, which in this case represent light being confined to the core. Thus, the resonant condition is the narrow band where light leaks out of the core, and it does so with very high loss. To obtain these loss wavelengths, consider the transverse phase difference between rays at locations A and B in Fig. 1 (a). The phase-matching condition for resonance occurs when this phase difference is an integer multiple ℓ of 2π , which can be written $2w\beta_{\perp} = 2\pi\ell$, where β_{\perp} is the transverse propagation constant in the capillary and w is the thickness of the capillary. Such cases can be thought of as standing wave solutions inside the glass layer. After a straightforward derivation in terms of the parameters given in Fig. 1 (a), we find that, consistent with the results of the ARROW model [19],

$$\lambda_{\ell} = \frac{2wn_2}{\ell} \sqrt{1 - \left(\frac{n_1}{n_2}\right)^2 (1 - \sin^2(\phi))} \quad \ell = 1, 2, \dots, \quad (7)$$

where λ_{ℓ} is the resonant (or ‘loss’) wavelength and the other parameters are defined in the figure. The $\sin^2(\phi)$ in the square-root can often be neglected, since as suggested by Duguay [18] for small angle ϕ we have the approximation $\sin(\phi) \approx \lambda_{\ell}/(4n_1r_{core})$ (for fibre core radius r_{core}), which in the limit $r_{core} \gg \lambda_{\ell}$ becomes small and so can be ignored. Eq. (7) highlights the dependence of the capillary thickness and core index n_1 on these high-loss wavelengths, which will be used in later sections. Between the high-loss wavelengths, we expect broad transmission bands for when this strict resonant condition isn’t satisfied. In real fibres the loss region is often less sharp due to small variations in the capillary thickness and the gap between resonators along the fibre as a result of instabilities in the fabrication process.

3.2 Modelling dispersion in HCF

The model we use is based off that developed by Zeisberger *et al.* [9] in which the authors considered an annular AR-HCF design of a single capillary of thickness w around a central glass-free core (i.e. the dashed ring in Fig. 1 (b)). For the HE_{11} fundamental mode, the effective index n_{eff} has the analytic expression

$$\Re(n_{eff}) = n_{gas} - \frac{j_{01}^2}{2\beta_0^2 n_{gas} r_{core}^2} - \frac{j_{01}^2}{\beta_0^3 n_{gas}^2 r_{core}^3} \frac{\cot(\phi)}{\sqrt{\varepsilon - 1}} \frac{\varepsilon + 1}{2} \quad (8)$$

$$\Im(n_{eff}) = n_{gas} \frac{j_{01}^3}{2} \frac{\varepsilon^2 + 1}{\varepsilon + 1} (1 + \cot(\phi)) \left(\frac{1}{\beta_0 n_{gas} r_{core}} \right)^4, \quad (9)$$

where n_{gas} is the filling gas of the fibre (see Section 3.3), r_{core} is the radius of the annular ring, β_0 is the vacuum propagation constant, j_{01} is the 1st root of the Bessel function j_0 , and ε and ϕ have the following expressions

$$\varepsilon = \left(\frac{n_{wall}}{n_{gas}} \right)^2 \quad \phi = \beta_0 w \sqrt{n_{wall}^2 - n_{gas}^2}, \quad (10)$$

with n_{wall} being the index of the capillary (where we have used fused-silica throughout). Although the dispersion function of a revolver-type HCF is well-described by the annular model, as shown by Song *et al.* [20] a better approximation can be achieved by accounting for the larger effective core radius introduced as a result of the negative curvature through

adjusting the value for j . More precisely, by considering the geometry in Fig. 1 (b), we obtain an expression for the normalised closest gap, $\gamma = g/r_{core}$, between neighbouring capillaries in an M -ring revolver type HCF through

$$\gamma = 2 \left[\sin \left(\frac{\pi}{M} \right) + \left(\sin \left(\frac{\pi}{M} \right) - 1 \right) \left(\frac{r_{cap} + w}{r_{core}} \right) \right]. \quad (11)$$

A generally good approximation for the capillary radius r_{cap} in the absence of more precise information is $0.7r_{core}$. We then relate γ to the adapted value for j using the results of Song *et al.*. Fig. 2 shows the dispersion and loss for a fibre with core radius $22 \mu\text{m}$ and capillary thickness $0.7 \mu\text{m}$. The resonance wavelengths are marked on the figure for the first, second and third resonances, as predicted by the ARROW model in Eq. (7).

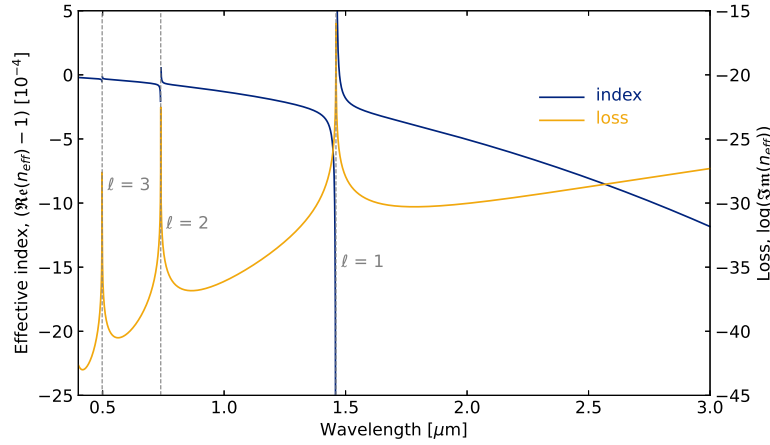


Figure 2: The real and imaginary parts of the effective index for a HCF with model parameters $r_{core} = 22 \mu\text{m}$ and $w = 0.7 \mu\text{m}$. Marked on the plot with vertical dashed lines are the wavelengths satisfying the resonance condition of Eq. (7) for the ARROW model.

3.3 Extending the model: Gas-filled HCF

We wish to extend the model to incorporate the effects of filling the hollow-core with a noble gas of our choosing. Work by Börzsönyi *et al.* [21] based on measurements of the dispersion of different noble gases at initial pressure ($p_0 = 1000 \text{ mBar}$) and temperature ($T_0 = 273 \text{ K}$) then goes on to develop a model to describe the wavelength-dependent dispersion of these gases at different pressures p (units mBar) and temperatures T (units K), which they verified between the UV and near IR regime. The expression they derived is

$$n_{gas}^2(\lambda, p, T) - 1 = \frac{p}{p_0} \frac{T_0}{T} \left[\frac{B_1 \lambda^2}{\lambda^2 - C_1} + \frac{B_2 \lambda^2}{\lambda^2 - C_2} \right] \bigg|_{(p_0, T_0)} \quad (12)$$

where n_{gas} is the real effective index of the gas, B_1 , B_2 , C_1 and C_2 are constants for the specific gas, reported in [21], and λ is the wavelength in nm.

So long as the gas index does not exceed that of the capillaries ($n_{gas} < n_{wall}$), the model of the HCF index considered in the previous section still holds, and we simply substitute in

the expression for the gas index. We also point out here that in Section 6 we apply this index to the mid-IR. We have assumed for this report that this model maintains a good level of accuracy in that regime, however alternative index models could be implemented to improve the full simulations in the future.

4 Methods for Measuring Fibre Dispersion

In this section, we introduce spectral interferometry (SI), a linear technique relying on a spectral phase difference between two overlapped pulses. After stating the theory of SI, we describe two methods for measuring the dispersion of optical fibres.

4.1 Theory of spectral interferometry

When two pulses are recombined in an interferometer setup, spectral interference occurs. If one pulse accumulates an additional phase compared to the other, a fringe pattern can be observed in the combined spectrum, which depends on this difference in phase. In Section 4 we will describe our experimental set-up and also the origin of this phase difference in practice. For now, consider two replicas of a laser pulse $\hat{E}(\omega)$ which travel along different beam paths and are recombined at a spectrometer for their combined spectrum to be analysed. We assume the necessary conditions of spatial overlap and equal polarisation are satisfied. Denote \hat{E}_1 and \hat{E}_2 as the fields from each beam when recombined, accounting for losses along propagation. For the real phase, we write the phase difference between the pulses as Φ and apply it to one of the fields without loss of generality. Then the intensity I at the spectrometer (OSA) is, by the superposition principle,

$$I(\omega) = \left\| \hat{E}_1 + \hat{E}_2 \exp(i\Phi) \right\|^2 \quad (13)$$

which can be simplified to

$$I(\omega) = \left\| \hat{E}_1 \right\|^2 + \left\| \hat{E}_2 \right\|^2 + 2 \left\| \hat{E}_1 \hat{E}_2 \right\| \cos(\Phi) \quad (14)$$

$$= I_1 + I_2 + 2\sqrt{I_1 I_2} \cos(\Phi) \quad (15)$$

where the last term in (15) is the so-called *interference* term. If we assume $\left\| \hat{E}_1 \right\| = \left\| \hat{E}_2 \right\|$, then this further reduces to

$$I(\omega) = 4I_0 \cos^2 \left(\frac{\Phi}{2} \right). \quad (16)$$

4.1.1 Zero-delay frequency

Even though the beams travel different paths, there may exist frequencies within the spectra for which the arrival time of the same frequency matches exactly. Such a frequency ω_0 is thus a solution to when the GD is zero, i.e. $\partial\Phi/\partial\omega|_{\omega_0} = 0$. We will refer to these frequencies as *zero-delay frequencies* (sometimes it is convenient to refer to them as *zero-delay wavelengths* which is justified since the map $\omega \leftrightarrow \lambda$ is unique). To not get this confused with the zero dispersion wavelength which would have the same abbreviation, we will not abbreviate it. These frequencies are sometimes important in analysing the spectral interferogram since they appear as points of inflection – this is the basis for the technique described in the next section.

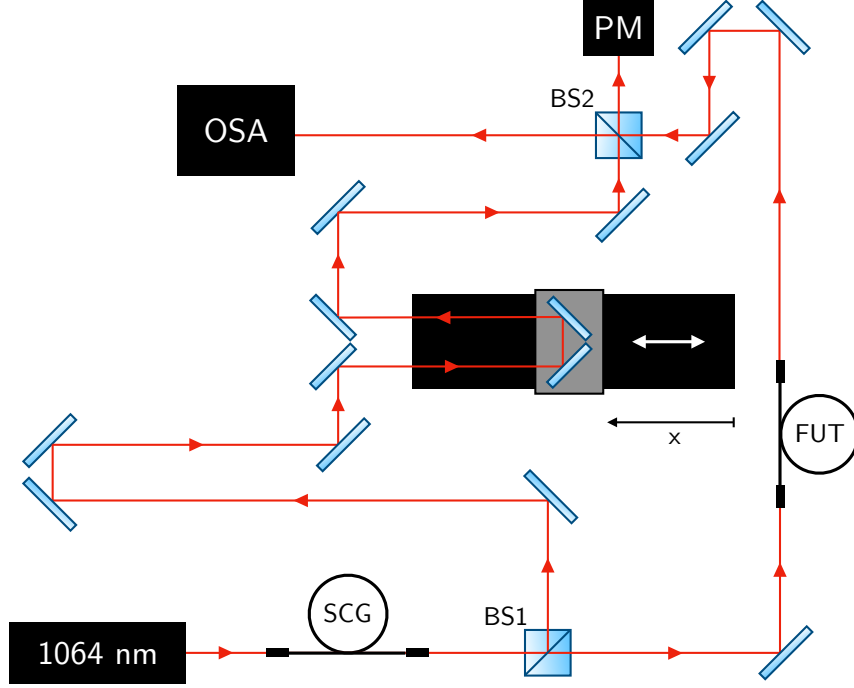


Figure 3: A Mach-Zehnder interferometer is used as the dispersion measurement setup. The translation stage can be used to change the delay between the arms. BS1 and BS2 are 50:50 beamsplitters; OSA is an optical spectrum analyser; SCG represents the super-continuum generation in fibre; FUT is the fibre under test and PM is a power meter.

4.2 Manual dispersion measurement

In this section, we describe a manual interferometric method used to measure fibre dispersion by introducing a variable delay τ and recording the change in location of a zero-delay wavelength in the output spectrum [22].

In this section only, the measurement was conducted using a silica-based photonic crystal fibre (PCF). This is because the method exploits a relatively high dispersion accumulation in the spectral phase for the point of inflection to be trackable. Since HCFs have low dispersion, a long fibre length would have been necessary, substantially increasing the size of the interferometer, and making it impractical.

In both this section and Section 4.3, we consider the experimental set-up in Fig. 3. The laser source was a broadband ($\Delta\lambda \sim 1 \mu\text{m}$) super-continuum generated in a micro-structured PCF and was seeded by a pump laser. The beam was then directed into a Mach-Zehnder interferometer with a fibre under test (FUT) in one arm. The other arm contained a translation stage to allow manual control of the delay between the arms by up to 60 cm. After propagating through the respective arms, the light was combined at BS2 with this light then coupled into a fibre, which was sent to the OSA. In this case, there were two contributions to the phase difference between the pulses: A constant temporal delay and a difference in dispersion. The delay was due to a mismatch in the optical path lengths in air and the dispersion difference was dominantly due to the FUT (we assumed the air and

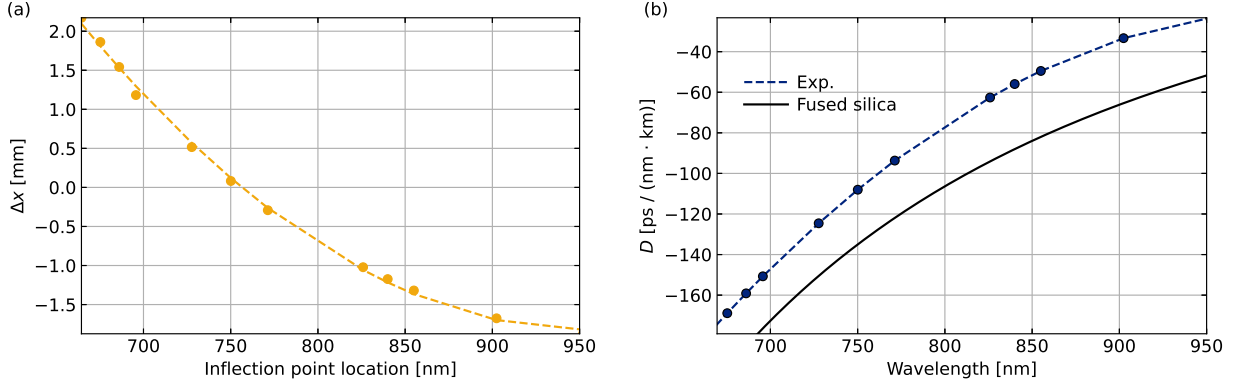


Figure 4: (a) How zero delay wavelength in spectrum varies with stage position. (b) GVD calculated from manual dispersion data and Eq. (20) compared to the GVD of fused silica calculated from its Sellmeier coefficients.

optical elements[†] were non-dispersive).

For a fixed delay τ , by the Fourier time-shift formula, the spectrum of the delayed pulse will accumulate phase $\omega\tau$. The dispersion of the fibre adds spectral phase which we label $\Delta\varphi$. The total difference in phase between the pulses will be the sum of these contributions,

$$\Phi := \omega\tau + \Delta\varphi \equiv \beta_0(\omega)[\Delta L_{air} + n_f(\omega)L_f], \quad (17)$$

where β_0 (units m^{-1}) is the vacuum propagation constant, ΔL_{air} (units m) is the difference in air between the two arms, n_f is the real effective index of the FUT and L_f (units m) is the length of the FUT. Since Φ is the phase *difference*, it is independent of the initial phase of the pulses. From this closed-form expression for Φ , we see that a zero-delay wavelength λ_0 satisfies

$$\Delta L_{air} = -L_f n_g(\lambda_0), \quad (18)$$

where $n_g := n_f - \lambda n'_f$ is the (real) *group index* of the fibre. We can see that by changing ΔL_{air} , λ_0 changes, and thus so does the location of the point of inflection in the spectrum.

Next, we describe the method. By incrementing the translation stage position, x , we add a delay τ to all frequencies in the pulse in the delay arm, shifting the location of the zero delay frequency in the spectrum, which was recorded. The amount a given zero-delay frequency shifts in the spectrum depends on the index of refraction of the fibre. We first define an origin ($x = 0$) for where this translation is measured from. Then for an arbitrary measurement position x_m of the stage from this origin, we will have zero delay for any wavelength such that the time travelling through each arm is equal, i.e.

$$L_d + 2x_m = L_a + n_g(\lambda_0)L_f, \quad (19)$$

[†]When measuring HCF, the dispersion is so low that we need to be careful to account for the dispersion in the focusing elements used to couple into the FUT. This will be accounted for in Section 4.3.

where L_d is the length of the delay arm when $x = 0$, L_a is the length of the air path in the fibre arm, and $n_g L_f$ is the optical path length of the FUT. The factor of two comes from the fact the light double passes the single distance x_m of the stage. We can relate the group velocity to the group index in the fibre through $n_g = c_0/v_g$ and substitute into Eq. (19). Then we differentiate with respect to wavelength and use Eq. (6) to obtain

$$\left. \frac{dx_m}{d\lambda} \right|_{\lambda=\lambda_0} = \frac{c_0 L_f}{2} \cdot \text{GVD}(\lambda_0), \quad (20)$$

where λ_0 is the location of the point of inflection in the spectrum. This is precisely a relationship that allows us to compute the GVD (units ps/(nm · km)) by only measuring the point of inflection and changing the delay. Figs. 4 (a) and (b) show the results of this measurement and the calculated GVD for a PCF of length $(0.575 \pm 1 \times 10^{-3})$ m. Since the dispersion of the PCF is dominated by the dispersion of the silica glass which the light propagates within, we have plotted the measurement alongside the GVD of fused silica. We expect the difference between the silica GVD and the measurement is mostly due to waveguide dispersion which we have not estimated. Due to the presence of the 1064 nm pump, the uncertainty in the point of inflection reading was higher at longer wavelengths due to a reduction in contrast of the interference fringes around the peak.

We have demonstrated that this method is robust and simple, however, as mentioned it relies on a relatively high GVD. In the following section we therefore describe an alternative method applicable to fibres with low dispersion, including HCFs.

4.3 Fourier transform spectral interferometry

The other technique for extracting the dispersion of optical fibres is Fourier transform spectral interferometry (FTSI). A full theoretical treatment of this method was presented by Takeda *et al.* [23]. This technique in principle results in a full retrieval of the spectral phase difference $\Delta\varphi$ due to fibre dispersion which, as seen in Eq. (15), is completely contained in a single interference trace. Work by Dorrer *et al.* [24] discusses many of the challenges of this method in practice, and suggests a minimal requirement of converting the spectrum to the angular frequency domain by linear interpolation. We consider the trace described by Eq. (15) written in the following form

$$I(\omega) = (I_1 + I_2) + \sqrt{I_1 I_2} \left[\exp(i\omega\tau) \exp(i\Delta\varphi) + c.c. \right], \quad (21)$$

where *c.c.* is the complex conjugate. Then, applying a Fourier transform takes us to the ξ domain. The numerical analog to this is the use of the Cooley–Tukey fast Fourier transform (FFT) algorithm (see Figs. 5 (a) and (b)). The first term in Eq. (21) contributes a DC spike (at $\xi = 0$) and the Fourier-shift formula tells us, for sufficiently large τ , we expect distinguishable side-bands centered on τ . More precisely, we obtain

$$\hat{I}(\xi) = \mathcal{F}\{I_1 + I_2\} + \sqrt{I_1 I_2} \left[\mathcal{F}\{\exp(i\Delta\varphi)\}(\xi + \tau) + \mathcal{F}\{c.c.\}(\xi - \tau) \right]. \quad (22)$$

Selecting a single side-band thus isolates $\mathcal{F}\{\exp(i\Delta\varphi)\}$, which we re-center, and inverse Fourier transform. In practice, this can be achieved by multiplying by a box-filter function between two bounds in the ξ domain which can be specified (see Fig. 5 (b)) and applying

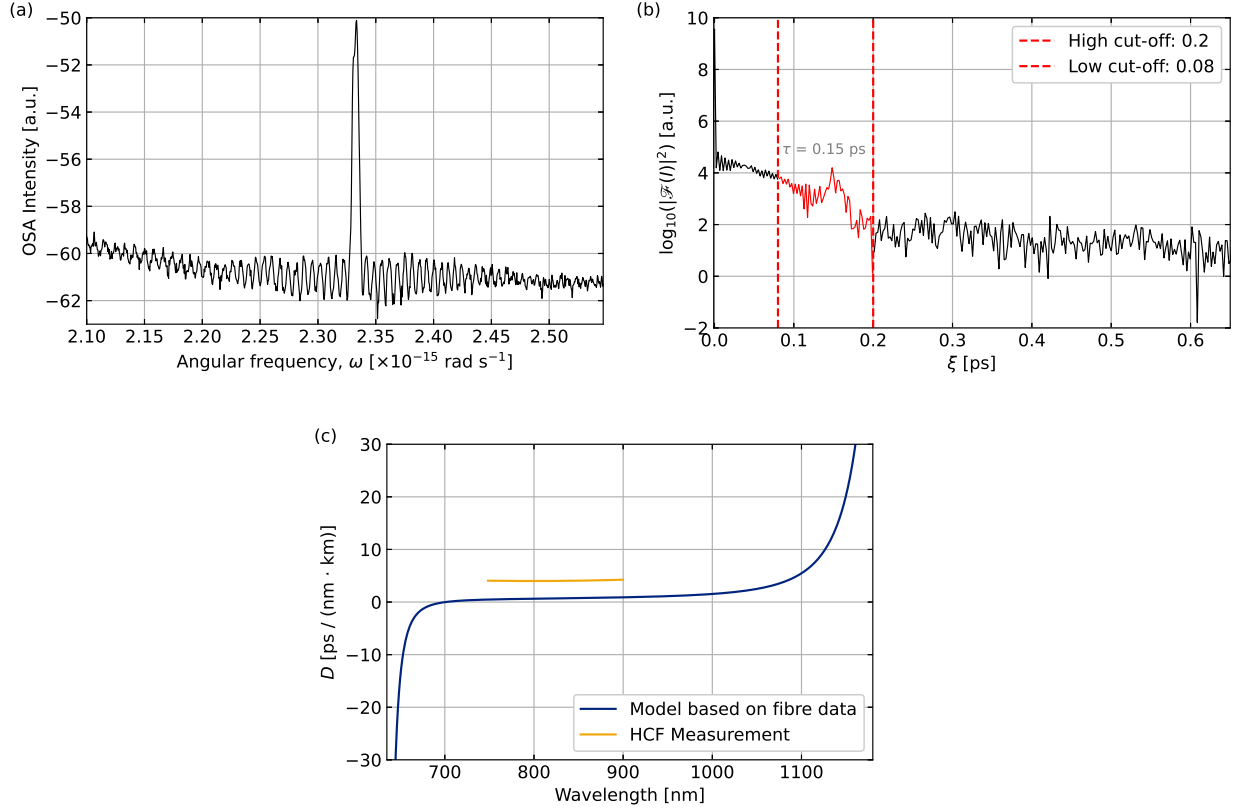


Figure 5: (a) Spectral interference trace for a 6-ring HCF plotted in the frequency domain after linear interpolation. Note that the spike around $2.33 \times 10^{15} \text{ rad s}^{-1}$ is due to the pump of the laser that was used. (b) Fourier transform of the trace into ξ domain limited to $\xi > 0$, with selected side-band between low and high cut-off lines. The estimated delay between the beams is 0.15 ps, which is the displacement of the side-band from zero. (c) The calculated GVD from the measurement, compared to the HCF model with parameters $r_{\text{core}} = 24 \text{ } \mu\text{m}$, $w = 0.6 \text{ } \mu\text{m}$, $M = 6$.

an FFT-shift and inverse-FFT to the result – both of these are available in any numerical library. The resulting phasor has argument $\Delta\varphi$, and so taking a complex logarithm retrieves it. The final step is to unwrap this phase since there may be discontinuous steps of 2π as a result of the numerical routines used.

We used this method to measure the dispersion of a 6-ring revolver-type HCF of length $(1.220 \pm 1 \times 10^{-3}) \text{ m}$ with quoted core radius $24 \text{ } \mu\text{m}$. To extract the GVD, we first performed a polynomial fit to the extracted phase – using the lowest order polynomial which fits the phase helps to minimise error when subsequently differentiating. We then computed the GD data, and subtracted from this the GD data separately measured for the microscope objective lenses used in coupling into the fibre. We differentiated the result using a numerical centered-difference and divided by the measured fibre length. Fig. 5 (c) shows the measurement compared to the GVD from the model with the parameters chosen based on the manufacturing data. We see good general agreement in the data, however the GVD we measured is offset by approximately $4 \text{ ps}/(\text{nm} \cdot \text{km})$ across the entire measurement range. We speculate that this is likely a combination of errors introduced through the fits used in the numerical routines, uncertainty in the lens GD data, and a background noise level present in

the ξ domain.

Fig. 5 (c) highlights some of the notable features of the HCF GVD. Namely that between resonances the GVD is flat and slightly anomalous for most of the transmission band, except close to resonances where the GVD changes rapidly. Within each transmission band we see the existence of a ZDW, where the GVD crosses through zero.

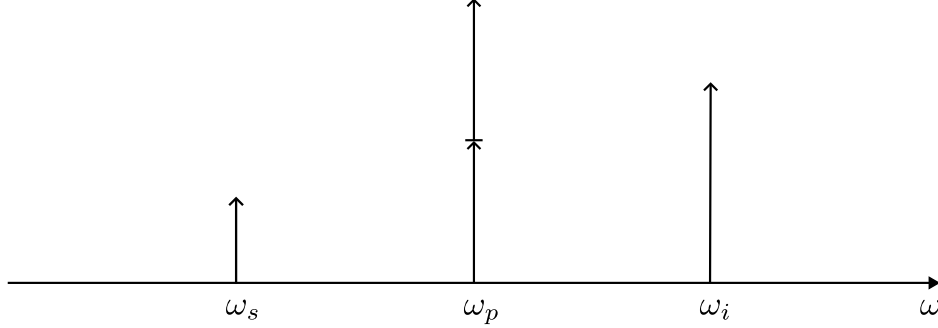


Figure 6: An illustration of the waves in degenerate four-wave mixing; the signal and idler frequencies which are generated are equally spaced in frequency from the pump.

5 Four-wave Mixing

5.1 Introduction to nonlinear optics

Dielectrics become polarised in response to an applied electric field. For linear dielectrics, the material response is linear in the electric field \mathbf{E} , and the first-order electric susceptibility $\chi^{(1)}$ describes the response of the material. This picture explains the linear dispersion in terms of a driven harmonic oscillator, where different frequencies receive different phase delays. At higher intensities, such as those in a laser, the response deviates from this linear picture in a way that, in general, can be understood through a power series expansion of the polarisation \mathbf{P} in the electric field [25]

$$|\mathbf{P}| = \varepsilon_0(\chi^{(1)}|\mathbf{E}| + \chi^{(2)}|\mathbf{E}|^2 + \chi^{(3)}|\mathbf{E}|^3 + \dots). \quad (23)$$

Here, we have illustrated the expansion to motivate the origin of the nonlinear electric susceptibilities $\chi^{(2)}$ and $\chi^{(3)}$, however, in the full vector description $\chi^{(n)}$ is a tensor of rank $n + 1$. Further, in the complete picture, the polarisation response is not instantaneous and is described through a convolution of the electric field with time-dependent susceptibilities.

Nonetheless, the important point is that the $\chi^{(2)}$ and $\chi^{(3)}$ susceptibilities are responsible for many of the nonlinear parametric optical processes that are commonly used in the laboratory today, and each of them is responsible for a distinct family of processes.

Processes permitted by the $\chi^{(2)}$ susceptibility are second-harmonic generation (SHG) [26], sum-frequency generation (SFG) and difference-frequency generation (DFG) – the latter is also known as optical parametric amplification (OPA) as the difference-frequency photon produced is facilitated by the generation of another photon at the lower input frequency. All of these processes can only occur in materials that lack an inversion symmetry called centro-symmetry. However, in the case of isotropic media which do possess this symmetry, such as silica glasses used in optical fibres and noble gases, their $\chi^{(2)}$ vanishes. This means

that, for our purposes, we can ignore any such $\chi^{(2)}$ process as it will have zero conversion efficiency [27].

On the other hand, $\chi^{(3)}$ processes can still occur irrespective of the centro-symmetry condition. Nonlinear processes resulting from the third-order susceptibility include third-harmonic generation (THG), the intensity-dependent refractive index – often leading to self-focusing via the optical Kerr effect – and four-wave mixing (FWM).

The silica used in optical fibres does possess a small $\chi^{(3)}$ nonlinearity [28], however due to the guidance mechanism the overall nonlinearity of the HCF is small. Filling the fibres with noble gases allows us to increase the nonlinearity [29, 30], increasing the efficiency of the FWM process in the fibres we consider.

Note also that all of these processes in which new fields are generated, both in the $\chi^{(2)}$ and $\chi^{(3)}$ case, are subject to the appropriate phase-matching condition.

5.2 Scalar theory of four-wave mixing

We now provide more detail into the process we are interested in, FWM. If we assume equal polarisation and colinearity between all waves, we can describe the process using scalar theory. If energy and momentum are conserved, two input waves can be annihilated and two distinct output waves can be generated. The phase-matching requirement means that in general care must be taken to ensure that the process can take place, but if it does the conversion efficiency in fibres can be relatively high due to the long interaction distance along the fibre. In this report, we consider *degenerate* FWM, whereby the two input waves are of the same frequency and thus the process can occur due to a single pump beam. The energy conservation equation between the four waves is then simply written

$$2\omega_p = \omega_s + \omega_i, \quad (24)$$

where ω_p is the pump frequency and ω_i and ω_s are the generated frequencies known as the idler and signal respectively. As photon energy is linear in frequency, it is easy to see that the generated waves are equally spaced by $\Delta\omega$ from the pump (see Fig. 6). From Eq. (24), we can see that the solution set is infinite. The phase-matching restriction is therefore imposed by the more sensitive condition of momentum conservation. We write the momentum mismatch between the four waves as

$$\Delta\beta = 2\beta_p - \beta_s - \beta_i - 2\gamma_{\text{NL}}P_0, \quad (25)$$

where efficient FWM conversion therefore only occurs if Eq. (24) is satisfied and Eq. (25) is minimised. The $2\gamma_{\text{NL}}P_0$ term in Eq. (25) is a nonlinearity term that occurs due to the nonlinearity of the refractive index at high-powers. At the powers we initially consider in this work this term is relatively small, and so we set it to zero in our simulations.

5.2.1 Phase-matching in hollow-core fibre

To solve Eq. (25) numerically, we first constructed matrices out of pump and signal frequency arrays and computed an idler matrix by use of Eq. (24). Then, a matrix representing $\Delta\beta$'s was computed by converting each of these matrices into matrices of β 's using $\beta = n_{\text{eff}}(\omega)\omega/c$ where n_{eff} was the effective index from the model. The optimum phase-matching solutions correspond to when $\Delta\beta$ is minimised, so a contour of this minimum was computed.

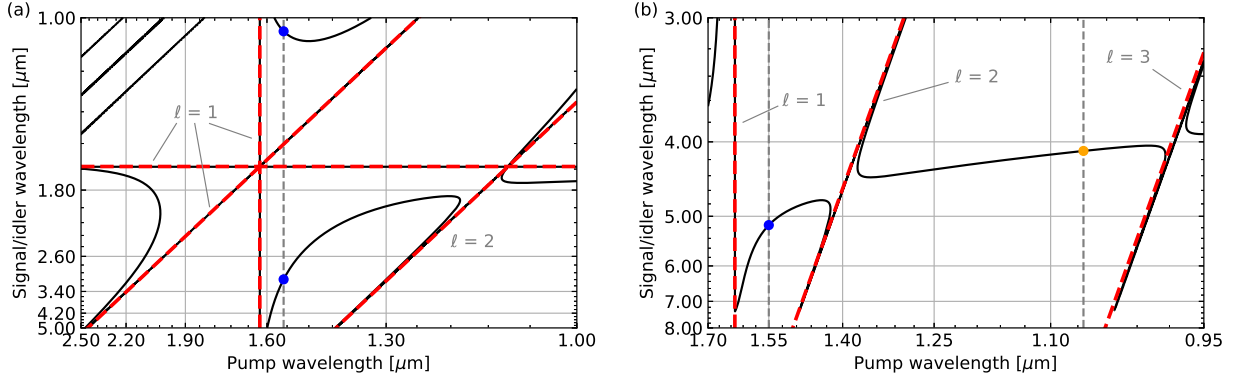


Figure 7: In both plots, the fibre parameters are: $r_{core} = 15.0 \mu\text{m}$, $w = 0.780 \mu\text{m}$, gas = argon, $p = 5000 \text{ mBar}$, $T = 293 \text{ K}$. (a) FWM phase-matching with solution pair highlighted for $\lambda_p = 1.55 \mu\text{m}$ at (blue spots) $\lambda_i = 1.04 \mu\text{m}$ and $\lambda_s = 3.07 \mu\text{m}$. (b) The phase-matching changes when the nonlinearity term $2\gamma_{NL}P_0$ is ‘turned on’. Here we set $2\gamma_{NL}P_0 = 5000 \text{ m}^{-1}$ and observe the phase-matching solution for the $1.55 \mu\text{m}$ pump increase to $5.20 \mu\text{m}$ (blue spot) and a new solution in the mid-IR at $4.10 \mu\text{m}$ (yellow spot) for a $1.064 \mu\text{m}$ pump. Red dashed lines correspond to loss regions verified through the ARROW model (Eq. (7)).

Fig. 7 (a) shows an example of these solutions for specified fibre parameters which will be discussed in the next section. For now, it is informative to highlight that the red dashed lines in the figure are the resonances of the ARROW model ($\ell = 1, 2$), which are plotted for the pump frequencies, signal frequencies, and the idler frequencies – the idlers are computed through the energy conservation equation, Eq. (24).

6 Simulation Results

Using the techniques described previously, we sought solutions to the FWM equations which produced a signal photon in the mid-IR. We investigated three commercially available pump wavelengths: 800 nm, 1064 nm, and 1550 nm. By far the most favourable pump for longer wavelength solutions was 1550 nm, primarily due to the smaller $\Delta\omega$ between the pump and signal and idler, which can be achieved with a less rapidly changing dispersion. Since such rapidly changing dispersion inevitably occurs close to the loss wavelengths in HCF, the solutions are inherently lossy.

By optimising over realistic parameter ranges, we present a $3.07 \mu\text{m}$ solution for a $1.55 \mu\text{m}$ pump in Fig. 7 (a). This solution provides the best balance we could find between separation from the resonance and far detuning from the pump. The corresponding fibre parameters for this solution are given in the figure caption. We see that for solutions between the $\ell = 1$ and $\ell = 2$ resonances, the mid-IR solutions are ‘boxed in’, meaning high conversion efficiency seems to have a theoretical barrier with no solution for this configuration.

By manufacturing a smaller core radius, we can decrease the flatness of the GVD within each transmission band, but this comes at the cost of increasing the loss for longer wavelengths. A scaling rule for HCFs has been reported where larger fibre dimensions generally decrease loss for longer wavelengths [31]. For propagating the mid-IR solutions created in the FWM process, clearly, there exists a compromise between attaining the solution and ensuring

that more is not lost than is generated. For example, by reducing the core radius to 5 μm and keeping all other parameters fixed, we find a $\lambda_s = 4.27 \mu\text{m}$ solution is possible, however, the loss is expected to increase by a factor of 10^5 , rendering it undetectable.

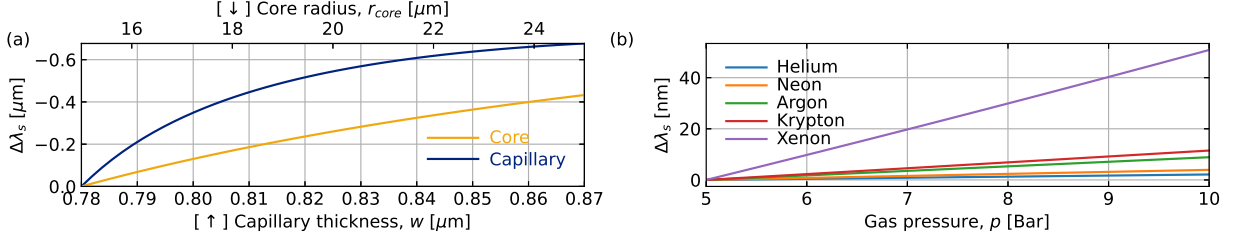


Figure 8: Phase-matching dependence on each parameter with $\Delta\lambda_s = \lambda_s^{(\text{new})} - \lambda_s^{(\text{initial})}$. (a) Both r_{core} and w are varied from their initial value given in Fig. 7. (b) The solution's dependence on gas type and pressure is shown.

A potential method to increase the conversion efficiency of the mid-IR solutions is by increasing the nonlinearity by increasing the power. In Eq. (25) we previously set $2\gamma_{\text{NL}}P_0 = 0$, however values between 100 m^{-1} and 5000 m^{-1} can push the phase-matching contour further into longer wavelengths. An initial investigation suggests that for $2\gamma_{\text{NL}}P_0 = 5000 \text{ m}^{-1}$ not only does the previous $3.07 \mu\text{m}$ solution increase to $5.20 \mu\text{m}$ with all other parameters remaining constant, but the phase-matched solution extends to the region between $\ell = 2$ and $\ell = 3$, providing a $4.10 \mu\text{m}$ solution for a $1.064 \mu\text{m}$ pump within the same fibre, as illustrated in Fig. 7 (b). Interestingly, the $1.064 \mu\text{m}$ pump solution exists farther from the loss regions, suggesting that it may be propagated with lower loss. Further, such values for the nonlinearity-power product would not be unrealistic in practice, since HCFs are well-known to be able to sustain high powers. A more thorough investigation will be necessary to explore this fully, for instance to account for differences in the gas index and evaluate the true nonlinearity γ_{NL} which would set the power requirement.

6.1 Dependence on model parameters

We also investigated the dependence of the $3.07 \mu\text{m}$ solution on the model parameters r_{core} , w , p and gas type. We found the solutions are particularly sensitive to the capillary wall thickness w , where nanometer changes can significantly impact the photon pair solution. Fig. 8 (a) shows that w changing by only 10 nm can lead to a shift in the signal of 200 nm.

Increasing gas pressure can be used to tune for higher phase-matching solutions, and it is clear that xenon is the best choice in this case. For instance, if w was manufactured to $0.790 \mu\text{m}$ whilst aiming for $0.780 \mu\text{m}$, a pressure of 45 bar could successfully compensate for the change to the phase-matching. The core radius is also a significant parameter since as mentioned it is responsible for changing the slope of the GVD. In absolute terms, we see that the dependence on core radius is hundreds of times less than the capillary thickness.

Typically, gas pressure tuning will only retrospectively compensate phase-matching solutions for a few tens of nm (see Fig. 8 (b)), which highlights the importance of high accuracy in fibre parameters. Such tuning will also impact the absolute loss of the solution, since the ARROW model explains the dependence of the loss wavelengths on the pressure-dependent index in the core. Since gas pressure/type will also affect the nonlinearity of the index, we

may expect them to become more prominent parameters if working to exploit the nonlinearity term in Eq. (25).

7 Conclusion and Outlook

In this report we have described two fibre dispersion measurement techniques based on spectral interferometry, along with their respective results. In both cases we see reasonable agreement to the expected GVDs, however we do believe a systematic error is responsible for an offset from the expected values in the case of the HCF dispersion measurement.

In Section 3 we described the HCF dispersion model developed by Zeisberger *et al.*, with a modification to incorporate some of the effects of negative curvature. We combined the HCF model with one of noble gas indices developed by Börzsönyi *et al.*, which varies with pressure and temperature. In Section 6, we solved the FWM energy and momentum conservation equations in the complete model of a gas-filled HCF. The results indicate that whilst the solutions exist in theory, further investigation should be undertaken to determine whether their conversion efficiency per unit length exceeds the losses in the mid-IR. We envision the next steps will be constructing satisfactory loss models to assess this. We have reported a 3.07 μm solution for a 1.55 μm pump as a good baseline for future investigations, and have shown how its existence depends on the model parameters. In addition, we indicate that further research with focus on the nonlinearity term $2\gamma_{\text{NL}}P_0$ in Eq. (25) may lead to more stable results with a greater conversion efficiency, since we have demonstrated that the solutions exist further away from any loss areas. Verifying the accuracy of the gas index model into the mid-IR will also be important before attempting to find these solutions in practice.

References

1. Le Corvec, M. *et al.* Fast and Non-Invasive Medical Diagnostic Using Mid Infrared Sensor: The AMNIFIR Project. *IRBM. TecSan 2012* **37**, 116–123. ISSN: 1959-0318 (Apr. 2016).
2. Kriesel, J. M. *et al.* Mid-IR hollow fiber gas sensor applications in environmental sensing and isotope analysis in *2022 Conference on Lasers and Electro-Optics (CLEO)* ISSN: 2160-8989 (May 2022), 1–2.
3. Takahashi, E. J. *et al.* Efficient laser wakefield acceleration by using mid-infrared pulses in *2018 Conference on Lasers and Electro-Optics (CLEO)* (May 2018), 1–2.
4. Flannigan, L. *et al.* Mid-wave and long-wave infrared transmitters and detectors for optical satellite communications—a review. en. *Journal of Optics* **24**. Publisher: IOP Publishing, 043002. ISSN: 2040-8986 (Mar. 2022).
5. Schneide, J. *et al.* Characterization of a Ho^{3+} -doped fluoride fiber laser with a 3.9 micron emission wavelength. EN. *Applied Optics* **36**. Publisher: Optica Publishing Group, 8595–8600. ISSN: 2155-3165 (Nov. 1997).
6. Mirov, S. *et al.* Progress in Cr^{2+} and Fe^{2+} doped mid-IR laser materials. en. *Laser & Photonics Reviews* **4**. eprint: <https://onlinelibrary.wiley.com/doi/pdf/10.1002/lpor.200810076>, 21–41. ISSN: 1863-8899 (2010).

7. Azhar, M. *et al.* Raman-free nonlinear optical effects in high pressure gas-filled hollow core PCF. EN. *Optics Express* **21**. Publisher: Optica Publishing Group, 4405–4410. ISSN: 1094-4087 (Feb. 2013).
8. Ciriolo, A. G. *et al.* Generation of ultrashort pulses by four wave mixing in a gas-filled hollow core fiber. en. *Journal of Optics* **20**. Publisher: IOP Publishing, 125503. ISSN: 2040-8986 (Nov. 2018).
9. Zeisberger, M. & Schmidt, M. A. Analytic model for the complex effective index of the leaky modes of tube-type anti-resonant hollow core fibers. en. *Scientific Reports* **7**. Number: 1 Publisher: Nature Publishing Group, 11761. ISSN: 2045-2322 (Sept. 2017).
10. Fox, M. eng. in *Optical Properties of Solids* (Oxford University Press, Incorporated, United Kingdom, 2010). ISBN: 978-0-19-957336-3.
11. Hooker, S. *Laser physics* eng. *Oxford master series in physics* **9**. ISBN: 978-0-19-850691-1 (University Press, Oxford, 2010).
12. Cregan, R. F. *et al.* Single-Mode Photonic Band Gap Guidance of Light in Air. *Science* **285**. Publisher: American Association for the Advancement of Science, 1537–1539 (Sept. 1999).
13. Knight, J. C. *et al.* All-silica single-mode optical fiber with photonic crystal cladding. EN. *Optics Letters* **21**. Publisher: Optica Publishing Group, 1547–1549. ISSN: 1539-4794 (Oct. 1996).
14. Pryamikov, A. D. *et al.* Demonstration of a waveguide regime for a silica hollow - core microstructured optical fiber with a negative curvature of the core boundary in the spectral region greater than 3.5 micron. EN. *Optics Express* **19**. Publisher: Optica Publishing Group, 1441–1448. ISSN: 1094-4087 (Jan. 2011).
15. Bradley, T. D. *et al.* Antiresonant hollow core fibre with 0.65 dB/km attenuation across the C and L telecommunication bands in 45th European Conference on Optical Communication (ECOC 2019) (Sept. 2019), 1–4.
16. Yu, F. & Knight, J. C. Negative Curvature Hollow-Core Optical Fiber. en. *IEEE Journal of Selected Topics in Quantum Electronics* **22**, 146–155. ISSN: 1077-260X, 1558-4542 (Mar. 2016).
17. Kosolapov, A. *et al.* Negative Curvature Hollow-Core Fibers (NCHCFs) for Mid-IR Applications in (July 2014).
18. Duguay, M. *et al.* Antiresonant Reflecting Optical Waveguides in SiO₂-Si Multilayer Structures. *Applied Physics Letters* **49**, 13–15 (Aug. 1986).
19. Litchinitser, N. M. *et al.* Antiresonant reflecting photonic crystal optical waveguides. EN. *Optics Letters* **27**. Publisher: Optica Publishing Group, 1592–1594. ISSN: 1539-4794 (Sept. 2002).
20. Song, P. *et al.* Quantitative analysis of anti-resonance in single-ring, hollow-core fibres. EN. *Optics Express* **27**. Publisher: Optica Publishing Group, 27745–27760. ISSN: 1094-4087 (Sept. 2019).
21. Börzsönyi, A. *et al.* Dispersion measurement of inert gases and gas mixtures at 800 nm. EN. *Applied Optics* **47**. Publisher: Optica Publishing Group, 4856–4863. ISSN: 2155-3165 (Sept. 2008).

22. Hlubina, P. Group velocity dispersion in fused-silica sample measured using white-light interferometry with the equalization wavelength determination. *Optik* **113**, 149–152. ISSN: 0030-4026 (Jan. 2002).
23. Takeda, M. *et al.* Fourier-transform method of fringe-pattern analysis for computer-based topography and interferometry. EN. *JOSA* **72**. Publisher: Optica Publishing Group, 156–160 (Jan. 1982).
24. Dorrer, C. *et al.* Spectral resolution and sampling issues in Fourier-transform spectral interferometry. *J. Opt. Soc. Am. B* **17**, 1795–1802 (Oct. 2000).
25. Boyd, R. W. *Nonlinear optics* Fourth edition. eng. ISBN: 978-0-12-811002-7 (Academic Press is an imprint of Elsevier, San Diego, 2020).
26. Franken, P. A. *et al.* Generation of Optical Harmonics. *Physical Review Letters* **7**. Publisher: American Physical Society, 118–119 (Aug. 1961).
27. Agrawal, G. P. *Nonlinear fiber optics* 5th ed. eng. ISBN: 978-0-12-397307-8 (Elsevier Science, Burlington, 2013).
28. Gubler, U. & Bosshard, C. Optical third-harmonic generation of fused silica in gas atmosphere: Absolute value of the third-order nonlinear optical susceptibility. en. *Physical Review B* **61**, 10702–10710. ISSN: 0163-1829, 1095-3795 (Apr. 2000).
29. Börzsönyi, Á. *et al.* Measurement of pressure dependent nonlinear refractive index of inert gases. EN. *Optics Express* **18**. Publisher: Optica Publishing Group, 25847–25854. ISSN: 1094-4087 (Dec. 2010).
30. Kolesik, M. & Wright, E. M. Universal long-wavelength nonlinear optical response of noble gases. EN. *Optics Express* **27**. Publisher: Optica Publishing Group, 25445–25456. ISSN: 1094-4087 (Sept. 2019).
31. Fokoua, E. N. *et al.* Loss in hollow-core optical fibers: mechanisms, scaling rules, and limits. EN. *Advances in Optics and Photonics* **15**. Publisher: Optica Publishing Group, 1–85. ISSN: 1943-8206 (Mar. 2023).